

Biomechanical assessment of bicuspid aortic valve phenotypes

Cruz De Oliveira, Diana; Abdullah, Nazirul ; Green, Naomi; Espino, Daniel

DOI:

[10.1007/s13239-020-00469-9](https://doi.org/10.1007/s13239-020-00469-9)

License:

None: All rights reserved

Document Version

Peer reviewed version

Citation for published version (Harvard):

Cruz De Oliveira, D, Abdullah, N, Green, N & Espino, D 2020, 'Biomechanical assessment of bicuspid aortic valve phenotypes: a fluid-structure interaction modelling approach', *Cardiovascular Engineering and Technology*, vol. 11, no. 4, pp. 431-447. <https://doi.org/10.1007/s13239-020-00469-9>

[Link to publication on Research at Birmingham portal](#)

Publisher Rights Statement:

This is a post-peer-review, pre-copyedit version of an article published in Cardiovascular Engineering and Technology. The final authenticated version is available online at: <https://doi.org/10.1007/s13239-020-00469-9>

General rights

Unless a licence is specified above, all rights (including copyright and moral rights) in this document are retained by the authors and/or the copyright holders. The express permission of the copyright holder must be obtained for any use of this material other than for purposes permitted by law.

- Users may freely distribute the URL that is used to identify this publication.
- Users may download and/or print one copy of the publication from the University of Birmingham research portal for the purpose of private study or non-commercial research.
- User may use extracts from the document in line with the concept of 'fair dealing' under the Copyright, Designs and Patents Act 1988 (?)
- Users may not further distribute the material nor use it for the purposes of commercial gain.

Where a licence is displayed above, please note the terms and conditions of the licence govern your use of this document.

When citing, please reference the published version.

Take down policy

While the University of Birmingham exercises care and attention in making items available there are rare occasions when an item has been uploaded in error or has been deemed to be commercially or otherwise sensitive.

If you believe that this is the case for this document, please contact UBIRA@lists.bham.ac.uk providing details and we will remove access to the work immediately and investigate.

**Biomechanical Assessment of Bicuspid Aortic Valve Phenotypes: A
Fluid-Structure Interaction Modelling Approach**

Diana M. C. de Oliveira*, Nazirul Abdullah, Naomi C. Green, Daniel M.
Espino

*Department of Mechanical Engineering, University of Birmingham, Birmingham B15
2TT, UK*

*Diana Marta Cruz de Oliveira; DMC795@student.bham.ac.uk

Acknowledgements

The authors wish to thank ARUP for providing the LS-DYNA and LS-PrePost licenses
for version R7.1.2.

Biomechanical Assessment of Bicuspid Aortic Valve Phenotypes: A Fluid-Structure Interaction Modelling Approach

Purpose: Bicuspid aortic valve (BAV) is a congenital heart malformation with phenotypic heterogeneity. There is no prior computational study that assesses the haemodynamic and valve mechanics associated with BAV type 2 against a healthy tricuspid aortic valve (TAV) and other BAV categories.

Methods: A proof-of-concept study incorporating three-dimensional fluid-structure interaction (FSI) models with idealised geometries (one TAV and six BAVs, namely type 0 with lateral and anterior-posterior orientations, type 1 with R-L, N-R and N-L leaflet fusion and type 2) has been developed. Transient physiological boundary conditions have been applied and simulations were run using an Arbitrary Lagrangian-Eulerian formulation.

Results: Our results showed the presence of abnormal haemodynamics in the aorta and abnormal valve mechanics: type 0 BAVs yielded the best haemodynamical and mechanical outcomes, but cusp stress distribution varied with valve orifice orientation, which can be linked to different cusp calcification location onset; type 1 BAVs gave rise to similar haemodynamics and valve mechanics, regardless of raphe position, but this position altered the location of abnormal haemodynamic features; finally, type 2 BAV constricted the majority of blood flow, exhibiting the most damaging haemodynamic and mechanical repercussions when compared to other BAV phenotypes.

Conclusion: The findings of this proof-of-concept work suggest that there are specific differences across haemodynamics and valve mechanics associated with BAV phenotypes, which may be critical to subsequent processes associated with their pathophysiology processes.

Keywords: bicuspid aortic valve; congenital malformation; fluid-structure interaction; multi-physics modelling

1. Introduction

A bicuspid aortic valve (BAV) is the most common form of congenital heart disease, affecting 1 to 2% of the global population [1]. In a BAV, two cusps are present instead of three (related to a “healthy” tricuspid aortic valve, TAV), being correlated with the onset of valvular pathologies such as aortic stenosis, regurgitation and calcification [2] and with several aortic diseases, such as dissection or dilation [1].

A BAV can be categorised as type 0, 1 or 2 [3]. Type 0 is linked to a pure BAV, composed of two distinct cusps. Type 1 has one fusion between two cusps. Given the left, right and non-coronary cusps present in the aortic valve, a BAV type 1 can have fusion between: the right-left (R-L) cusps, non-coronary-right (N-R) cusps and non-coronary-left (N-L) cusps. A BAV type 2, however, has two fusions: R-L and N-L [3]. These fusion patterns lead to heterogeneity between BAV phenotypes [3], associated with diverse patterns of flow asymmetry [4-6]. A study evaluating 1362 BAV patients found type 1 to be the most prevalent (79.15 %), followed by type 2 (12.41 %) and then type 0 (8.44 %), reporting similar mortality and morbidity [7]. However, clinical challenges differ: valve regurgitation has been correlated to type 1 R-L BAVs [7], while type 2 BAVs have been associated with the highest incidence of ascending aortic dilation [3, 7]. Further, BAV type 2 may direct valvar flow to the convexity of the ascending aorta, the typical location for onset of dilation (determining whether that increased local wall shear stress acts as a trigger for dilation onset and progress remains challenging) [3].

Computational models simulating BAV function have gained interest, as they predict haemodynamic factors not obtainable otherwise [8]. Fluid-structure interaction (FSI) methods have been employed to simulate aortic valve leaflet deformation and blood flow [9-14]. Previous FSI studies have focused either on BAV type 0 [15] or type 1 [16-18] in non-dilated aortas. These studies have used both two-dimensional [15] and three-dimensional [16, 17] idealized models, as well as patient-specific ones [18]. Such models have demonstrated the presence of eccentric and skewed ascending aortic flow, associated with vortices and abnormally high wall shear stress (WSS), when compared to a healthy tricuspid aortic valve (TAV). Other studies have studied the effect of asymmetric BAV models on blood flow [19] and even assessed how different nonfused cup angles in BAV type 1 impact on the valve’s structural and haemodynamic performance [20]. Despite reporting how the wide variation in BAV deformity impacts

on aortic blood flow, computational models have not taken into consideration BAV type 2, which undergoes an elevated incidence of dilation. It remains difficult to identify common features per BAV phenotype due to elevated clinical variability. However, the assessment of all BAV categories (including type 0, type 1 and type 2) is possible through computational modelling, but such a study has not yet been reported in the literature.

The aim of this study is to demonstrate proof-of-concept in developing a standardised platform for simulating and evaluating all BAV types (using the Sievers and Schmidtke categorisation). More specifically type 0 lateral and anterior-posterior, type 1 R-L, N-R and N-L and type 2, as well as a healthy TAV, are compared through a transient systolic FSI model. The objectives within this aim are to analyse the effect of BAV type 0 orifice orientation on aortic haemodynamics and valve mechanics; to determine whether raphe location in type 1 BAVs plays a significant role on blood flow, wall shear stress and valve stress; and to simulate for the first time a BAV type 2 model and assess its haemodynamic and valve mechanics.

2. Methods

2.1 Model geometries and grid settings

All models were generated using Solidworks 2013 (Dassault Systemes, Waltham, MA, USA). These consisted of idealised TAV and 6 BAVs with a constant thickness of 0.2 mm [9] representing: type 0 with lateral and anterior-posterior orientations, type 1 with R-L, N-R and N-L leaflet fusion and type 2. Cusps in BAVs type 1 and 2 were merged in the free edge, to represent the presence of a raphe (Figure 1). Dimensions employed for all models are presented in Table 1 and displayed in Figure 2, based on clinical measurements [21], consistent with other aortic valve studies [22], and previous BAV models [9, 15, 23]. As per previous studies [24, 25], the geometry of interest was the thoracic aorta, including aortic root, ascending aorta and aortic arch, with the model subsequently truncated at the descending aorta (Figure 3). The same diameter was assumed for ascending and descending aortas. As this study focused on flow at the aortic root and ascending aorta, aortic arch branches were neglected; their exclusion is not expected to alter flow profiles in the regions of interest as a previous FSI study which also excluded supra-aortic branches [26] predicted flow, such as peak flow velocities, consistent with clinical observations [27, 28].

[Table 1 near here]

[Figure 1 near here]

[Figure 2 near here]

[Figure 3 near here]

All geometries were meshed using ANSYS (Ansys Inc., Canonsburg, PA, USA) and one example is provided in Figure 3 a). Aortic models were based on a previously published study, which included mesh convergence analysis [23]; however, in FSI, the fluid ALE mesh shape conforms to the structural mesh, and fluid-solid mesh nodes are shared at the interface, meaning that any mesh refinement for one of the meshes results in a refinement of the mesh for the other domain at their interface. This may lead to a non-homogeneous mesh with implications for computational cost [29]. Therefore, mesh quality measures were the primary choice for model mesh assessment [30]. 20,900 hexahedral elements were created for the aortic model (fluid domain) to reduce computational time, while the valve leaflets (structural domain) were meshed with 5700 quadrilateral and triangular shell elements. The Belytschko-Lin-Tsay shell element formulation was employed to increase computational efficiency [31]. To avoid stepping artefacts in WSS which can occur with mesh refinement at boundary walls, no additional mesh refinement was added. A spatial resolution of 0.87 mm and 2.5 mm was then achieved for the structural and fluid meshes, respectively. Mesh quality was assessed through element skewness and orthogonal quality, which yielded average values of 0.2255 and 0.8832. According to quality criteria, the meshes had excellent skewness (between 0 and 0.25) and very good orthogonal quality (between 0.70 and 0.95) [30, 32].

2.2 Material properties and boundary conditions

Blood flow was approximated as a Newtonian and virtually incompressible fluid, a valid assumption for large scale flow in the cardiovascular system [33]. This material model was used in conjunction with the Grüneisen equation of state, which describes how volumetric changes affect the fluid reference pressure [32, 34]. The Grüneisen equation can be defined as:

$$p = \frac{\rho_0 C^2 \mu \left[1 + \left(1 - \frac{\gamma_0}{2} \right) \mu - \frac{a}{2} \mu^2 \right]}{\left[1 - (S_1 - 1) \mu - S_2 \frac{\mu^2}{\mu + 1} - S_3 \frac{\mu^3}{(\mu + 1)^2} \right]^2} + (\gamma_0 + a \mu) E, \quad (1)$$

where ρ_0 is the initial fluid density (1000 kg/m³); C is the elastic sound speed (set as 1500 m/s to increase blood's bulk modulus and make it a virtually incompressible fluid [35]); γ_0 is the Grüneisen parameter (1.65); a is the first order volume correction to γ_0 (0); S_1 , S_2 and S_3 are equation coefficients (1.79, 0, 0); E is the fluid initial internal energy (0 J). Blood flow compression is defined in terms of a relative volume V as:

$$\mu = \frac{1}{V} - 1 = \frac{\rho}{\rho_0} - 1, \quad (2)$$

where ρ is the blood density.

Linear elastic material properties were assigned to the aortic valve tissue, based on the reported range of cardiac tissue deformation [36-38] and previous studies [9, 15, 22, 39, 40]. The Young's modulus has been chosen to mimic valve behaviour as closely as possible. A density of 1000 kg/m³, a Poisson's ratio of 0.49 and a Young's modulus of 1.5 MPa were employed, based on a previous computational study [15]. The density of blood was set equal to that of the aortic valve to negate the effects of buoyancy, and its dynamic viscosity was assumed to be 4.3 mPa s [32, 33].

Time-dependent physiological flow conditions were applied at the aortic inlet and outlet (specified in Figure 3), with the inflow profile representing left ventricular ejection (Figure 4). These were modelled with spatially uniform velocity profiles. A fluid reference pressure of 80 mmHg was employed to simulate initial (diastolic) blood pressure. The aortic wall boundaries were assumed rigid and a no-slip condition was employed at the wall-blood interface. The same assumption was made for the TAV model, enabling like-for-like comparisons across BAV models. Similarly, a no-slip condition was enforced between the cusps and blood flow. Valve cusp edges were also fixed to constrain their movement within the aortic root.

[Figure 4 near here]

2.3 Fluid-structure interaction framework and study settings

The finite element software LS-DYNA 4.5.12 (LSTC, Livermore CA, USA) was used to implement and solve the FSI between blood flow and aortic valve cusp deformation. This software has been used previously for modelling aortic valve movement [22, 39-41]. An Arbitrary Lagrangian-Eulerian (ALE) formulation was chosen, where fluid

dynamics were solved using the continuity and incompressible Navier-Stokes equations (discretization of the fluid domain into solid LS-DYNA ALE fluid elements) and structural deformation using the linear elastic equation for isotropic, linear and elastic materials [42, 43]. Fluid flow was coupled to the valve structure by a penalty coupling method [32], similar to previous studies [22, 40, 41]. An hourglass control was also applied to prevent zero strain energy. The transient study was solved using the explicit hydrodynamic solver available in LS-DYNA and free-time stepping up to a total time of 0.8 s. Focus was given to the systolic phase of the cardiac cycle (referred to in the rest of this paper as 0 – 0.4 s), with results being obtained for this time period. All numerical simulations were performed on an Intel i7-9700 CPU with 16GB of DDR4 RAM workstation and took approximately > 30 hours to solve.

2.4 Mechanical and haemodynamic characterisations

Data post-processing was performed with LS-PrePost and MATLAB (R2017b v. 9.3.0, MathWorks, Natick, MA, USA). Von Mises stress was assessed at the valve cusps, while global aortic haemodynamics are reported for peak systole (time, $t = 0.125$ s) focusing on flow velocity, vortices, and pressure. Three cross-section planes were created for further haemodynamic quantification (planes B-B, C-C and D-D from Figure 3c.), their position similar to cross-sectional planes employed for 4D magnetic resonance imaging (MRI) measurements used *in vivo* [44].

Peak systolic transvalvular pressure across the aortic valve was obtained by calculating the averaged pressure before and after the valve (Equation 3),

$$\Delta P = P_u - P_d, \quad (3)$$

where P_u is the upstream pressure (aortic inlet boundary) and P_d is the downstream pressure (B-B cross-section).

Systolic retrograde flow was quantified at the cross-section B-B using MATLAB and through the systolic flow reversal ratio (FRR; Equation 4) index [45, 46],

$$FRR = \frac{|Q_n|}{|Q_p|} \%, \quad (4)$$

where Q_n and Q_p are the backward and forward flow rates at the cross-section of interest, respectively (when FRR equals 0, no retrograde flow is present). Surface integrals were defined for each element to determine the associated flow rate, as given by

$$Q = \int_{\Gamma} \mathbf{v} \cdot \mathbf{n} d\sigma, \quad (5)$$

where Γ is the finite element area of interest, t is the time instant, \mathbf{n} is the normal plane vector and σ is the finite element area limit, respectively.

The geometric (GOA) and effective (EOA) orifice areas were also calculated. The GOA was obtained by finding the planar area of each aortic valve orifice at peak systole. The EOA was calculated using a modified version of the Gorlin equation, written as:

$$EOA = \frac{Q_{rms}}{51.6\sqrt{\Delta P}}, \quad (6)$$

where Q_{rms} is the root mean square systolic flow rate (cm^3/s), ΔP is in mmHg and EOA is in cm^2 [47].

MATLAB was used to quantify WSS magnitudes at the defined cross-sections using equation 7,

$$WSS = \mu \frac{\mathbf{v} \cdot \mathbf{n}}{y}, \quad (7)$$

where μ represents the dynamic viscosity of the fluid, \mathbf{v} is the velocity vector and y is the perpendicular distance between each velocity vector and the aortic wall [44].

3. Results

3.1 Blood Haemodynamics

Peak velocity, transvalvular pressure drop, FRR and GOA and EOA results are presented in Table 2, listed along with published values for comparison.

3.1.1 Blood flow velocity and asymmetry

BAV models generated higher peak velocity magnitudes (> 2.2 m/s) in comparison with the TAV model (1.52 m/s). Among all BAVs, type 2 yielded the highest peak velocity value (3.7 m/s), while type 0 lateral generated the lowest (2.2 m/s), corresponding to a

150% and 38% increase when compared with the TAV, respectively. Type 1 BAVs predicted similar peak velocity magnitudes, regardless of raphe position.

While TAV generates a symmetrical and dispersed flow profile, BAV models give rise to an asymmetric distribution of the velocity field (Figure 5 and Supplementary Figure S1), characterized by the presence of concentrated high velocity flow. Flow direction varies according to the type of BAV; while elevated blood velocities are present at the centre of the ascending aorta in type 0, type 1 yields peripheral skewing of the systolic jet towards the aortic wall: BAVs R-L, N-R and N-L direct the jet towards the right-anterior, posterior and anterior portions of the ascending aortic wall, respectively. BAV type 2, instead, outputted the lowest flow volume of elevated peak systolic velocity in comparison with the remaining BAVs, associated with a greater flow constriction.

[Figure 5 near here]

[Table 2 near here]

The TAV generated mainly unidirectional flow in the ascending aorta, with the presence of small low velocity vortices (Figure 6). In all BAV cases, there was the development of stronger vortices with greater velocity in comparison with the healthy valve. Asymmetric flow is showed for type 0 and type 1 BAVs with the generation of counter-rotating vortices. Vortex spatial distribution was influenced by valve orifice location and the position of the raphe in type 1 BAVs, with two major vortices developing above the fused cusps. In BAV type 2, high velocity flow was directed towards the aortic wall, accelerating in opposite directions.

[Figure 6 near here]

3.1.2 Retrograde flow

Systolic retrograde flow was present in the ascending aorta in all BAV models ($> 3.5\%$), contrasting with the TAV (0%), as given by the FRR index (Table 2). The lowest FRR was predicted for type 0 lateral (3.5%), while type 2 yielded the highest FRR (13.3%). However, the presence of a raphe in type 1 BAVs gave rise to a higher generation of retrograde flow in comparison with the pure BAVs. Nonetheless, FRR values were similar among type 1 sub-phenotypes.

3.1.3 GOA and EOA

A reduction in GOA and EOA was observed for all BAVs in comparison with the tricuspid valve. According to clinical guidelines, the EOA for TAV is considered normal (3 - 4 cm²), while type 0 and 1 BAVs yielded EOAs which are considered mildly stenotic (1.5 – 2 cm²). While type 0 BAVs yielded the same EOA, type 1 BAVs were associated with higher EOA values, with the R-L phenotype having the lowest orifice area. BAV type 2 had the greatest reduction in EOA, corresponding to a moderate stenosis range (1 – 1.5 cm²).

3.1.4 Transvalvular pressure drop

The peak transvalvular pressure gradients predicted by the BAV models were greater than the one predicted by the TAV (4.5 mmHg). Among all BAV phenotypes, type 2 BAV gave rise to the greatest pressure drop (37 mmHg), with an increase of more than 700% from the pressure gradient obtained for the TAV. Both type 0 BAVs yielded the same transvalvular pressure drop (15 mmHg) and among type 1, the R-L phenotype was associated with the highest pressure drop (15 mmHg).

3.2 Characterisation of stresses

Peak systolic WSS (at the B-B cross section) and valve cusp Von Mises stress are listed in Table 3, along with published values. TAWSS and OSI have also been computed and made available in the Supplementary Figures S2 and S3. To avoid repetition in the analysis commentary, the main text in the sections below is focused on time-dependent results.

[Table 3 near here]

3.2.1 Wall shear stress

Peak systolic WSS magnitudes are displayed in Figure 7 for all models, across the ascending aorta. Type 0 BAVs yielded low WSS magnitudes; however, all other BAV models yielded greater WSS magnitudes in comparison with the TAV. The presence of a raphe in type 1 BAVs gave rise to higher WSS magnitudes in comparison with the pure BAVs, due to the eccentricity associated with the systolic flow jet and its direction towards the ascending aortic wall. The highest WSS magnitude was predicted for type 2

BAV (5.08 Pa), which is 10 times higher than the lowest WSS value for type 0 BAV. Type 1 and 2 BAVs gave rise to progressively decreasing WSS values along the ascending aorta, from the sinotubular junction (B-B section) to the distal regions (D-D section). Also, WSS magnitudes did not greatly vary within each BAV phenotype: type 0 BAVs generated similar WSS values along the ascending aorta and in type 1 BAVs, the WSS magnitudes corresponded to a standard deviation of only ± 0.2 Pa, showing that the position of the raphe does not greatly influence this magnitude amongst sub-phenotype categories.

[Figure 7 near here]

3.2.2 Cusps stress

Type 2 BAVs presented with the highest peak Von Mises stress (1.6 MPa - Table 4), almost 500% greater than the lowest BAV peak stress (BAV type 0 anterior-posterior; 0.27 MPa). Peak systolic Von Mises stress values were similar among type 1 BAVs. Increases in the area-averaged Von Mises stress from BAV models, in comparison with the TAV are displayed in Figure 8, focusing on the systolic acceleration phase and systolic peak. Although BAV type 0 anterior-posterior had a lower peak stress than TAV, its area-averaged stress was greater for the phases mentioned above. This is due to how the stresses are distributed across the cusp surfaces (Figure 9). Here, while the TAV model was associated with lower and more evenly distributed stresses, the BAV models displayed elevated and concentrated stresses at the constricted edges, more evident for BAVs type 1 and 2. Concerning type 0 BAVs, the valve orifice orientation influenced peak stress distributions on the cusps: while the lateral phenotype had more concentrated stress at the constricted edges adjacent to the orifice, such a feature was not present for the anterior-posterior configuration. Despite this, both phenotypes presented with marks of elevated stress at the middle of both cusp bellies. Type 1 BAVs presented with identical cusp stress distributions among one another, with concentrated stresses located at the raphe; nonetheless, phenotypes N-L and N-R also had high stresses at the belly of the non-fused cusp, adjacent to the valve orifice, coincident with the direction of the systolic flow jet for each case represented in Figure 5. This was not present, however, on phenotype R-L. Higher contour stresses were observed all over the cusps for BAV type 2, with the greatest stress located at the raphes near the valve orifice.

[Figure 8 near here]

[Figure 9 near here]

4. Discussion

4.1 Main study findings

FSI has been used to simulate congenitally malformed aortic valves. Type 0, 1 and 2 BAVs were simulated, including sub-classifications, and referenced against a TAV model. This approach enabled the first and object comparison of the key features of BAV type 2 against other BAV types and subcategories, as regards subsequent flow and stresses induced; only possible using idealised models. The obtained results suggest the following findings:

- The TAV model haemodynamic and mechanical predictions are consistent with those available *in vivo* [4, 6, 44, 48], *in vitro* [49, 50] and *in silico* [16, 17, 23, 46, 51] literature, therefore, validating our computational model;
- All BAV phenotypes induce abnormal haemodynamics in the aorta when compared to the TAV model;
- Concerning BAV phenotypes, type 0 has the lowest peak velocity magnitude, FRR, WSS magnitude and cusp stress, presumably leading to the least impact out of all types. The orientation of the valve in BAV type 0 influences the stress on the cusps in terms of maximum magnitude reached and its location, but global haemodynamic quantifications are not sensitive to its orientation. Regions of high and low WSS on the aorta, however, are determined by the orientation of the BAV type 0;
- The raphe location in type 1 BAVs influences the spatial distribution of haemodynamic features; nonetheless, these yield similar haemodynamic magnitudes (velocity and WSS) and valve stress values, regardless of the location of raphe.
- BAV type 2 exhibits the highest values in haemodynamic parameters (peak velocity, pressure gradient and FRR) and lowest GOA and EOA, as well as highest valve stresses, presumably leading to the most damaging repercussions when compared to other BAV phenotypes.

4.2 Computational model validation and design framework

In this study, idealised geometries were used for the aorta and the aortic valve based upon clinical data and previous computational studies [9, 15, 21]. In reality, both geometric and functional factors related to aortic valve function are heterogeneous and no two patients present with the same morphological characteristics in a BAV population [52]. However, idealised computational modelling enables an unbiased comparison amongst BAV models not feasible clinically, such as the influence of valve orifice orientation on blood jet direction or the impact of the presence of a raphe in the overall cusp mechanics and haemodynamics.

All results for the healthy TAV model were in agreement with clinical measurements, *in vitro* experiments, and previous computational models: peak systolic velocity magnitudes differed by less than 35% and 20% when compared to other three-dimensional FSI models [16] and 4D MRI measurements [4-6], respectively. Indeed, some of this quantitative discrepancy would be accounted for by the specific differences in the models solved; qualitatively, all TAV model predictions were consistent with literature. For example, flow patterns with the development of small low velocity vortices were comparable to computational results presented elsewhere [53, 54].

Comparison of our TAV predictions with *in vivo* measurements was considered primordial and *in vitro/in silico* results were second choices of validation, due to the fact that any obtained data is subject to individual experimental bias or computational assumptions. Previous computational studies have used WSS magnitudes as a measure of the stress on the aortic valve cusps [55, 56]; however, this measure of stress only takes into account parallel forces acting on the valve surface. Thus, the Von Mises criterion was used as a measure of valve stress. WSS and Von Mises values predicted were consistent with previous computational studies modelling the TAV [16, 17, 51, 57].

4.3 Clinical impact of abnormal BAV haemodynamic and mechanical features

The BAV models were associated with lower GOA and EOA values, in comparison with the normal TAV, something which is expected to increase peak velocity and ΔP . Indeed, our models predicted an increase in most of the haemodynamic parameters studied, including peak systolic velocities, ΔP , FRR and WSS, as well as higher peak and average Von Mises stress on the valve cusps. These results further support the already well

established awareness that BAV is associated with abnormal ascending aortic haemodynamics [6, 16, 49].

The FRR predicted by type 0 BAV was much lower than the literature reports [46]; however, values in our study were derived from an FSI study whereas Bonomi et al. (2015) used CFD, with cusps in a single, fixed configuration.

The TAV ΔP value was consistent with the literature, while the values obtained for type 0 BAVs were 30% lower than previous *in silico* results (Table 2). Nonetheless, the reduced valve systolic orifice associated with our BAVs yielded consistently greater ΔP than the TAV, in agreement with the literature [58]. According to the obtained EOA, their configuration is considered mildly (types 0 and 1) or moderately (type 2) stenotic [59-61], even without cusp calcification or stiffening, which can overload left ventricular pressure with the potential for subsequent heart failure [62]. Moreover, all BAV models had elevated Von Mises stresses, which are associated with denudation of cusp endothelial cells, potentially leaving the valve susceptible to bacterial infections [63]. This information is relevant, because BAV patients have a greater propensity for infections. In addition, predicted cusp stresses increased with lower EOA, with BAV type 2 presenting with the highest stresses of all phenotypes. This suggests that type 2 BAV patients may be at greater risk of valve degeneration, which could result in severe aortic stenosis, heart tissue damage and myocardial infarction [64].

4.4 Different BAV phenotypes impact differently on aortic haemodynamics and mechanics

Previous computational studies have suggested that the elevated stresses present in BAV cusps can be associated with calcification development, leading to stiffer cusps, contributing to the obstruction of the left ventricular outflow [54, 65], as well as valve stenosis and aortic regurgitation [2]. Moreover, Conti et al. (2010) have noted increased stress at the belly region of a type 0 BAV model. Thus, and as per their results, the location of calcification onset may be sensitive to type 0 BAV orientation, due to the presence of peak stresses in different regions. Nonetheless, our type 0 BAVs presented with the lowest peak velocity and WSS magnitudes, FRR and Von Mises stress values, suggesting that, from all BAV phenotypes, this is likely the subtype with the least clinical impact.

Although Type 1 BAVs yielded different jet orientations with counter-rotating vortices, generating diverse spatial regions of elevated velocity (Figure 5), results suggest that raphe location does not have a great impact on blood peak velocity and WSS magnitudes and cusp stress, consistent with findings from Cao et al. (2017). However, these peak velocities were higher than the ones predicted for the TAV, also associated with increased average WSS in the ascending aorta. WSS is an important vascular regulator that can induce vascular remodelling by directly influencing endothelial cell function [66]. This then contributes towards aortic wall degeneration, associated with aortic dissection [67] and dilation [67, 68] and present in BAV patients [69]. Therefore, increased WSS in the ascending aorta may anticipate the onset of aortopathy and contribute to its triggering [24]; which is consistent with our present results that suggest increases in the average WSS along the ascending wall of aorta (measured at three distinct cross-sections along the wall of the ascending aorta). Clearly, this is an area which merits further investigation.

Type 2 BAV yielded what is presumed to be the most compromised haemodynamic and mechanical characteristics among all BAV phenotypes, including the highest peak systolic velocity and WSS magnitudes. It is hypothesised that BAV patients with worsened aortic stenosis might be at greater risk for aortic dilation onset and progression [70] and this may afflict individuals with a type 2 BAV in particular. Such a hypothesis is consistent with the current literature [3, 7] but clearly needs to be tested.

4.5 Clinical applications

The results obtained in this study show the importance of BAV patient stratification according to categories, since specific phenotypes differ in hemodynamic (peak velocity, FRR and pressure gradient) and mechanical measures (Von Mises stress, WSS). The use of indicators such as WSS may be useful to estimate the risk of dilation in BAV patients, by estimating phenotypes with a larger risk for dilation onset and progression. Aortic wall mechanics for BAV patients is fundamentally different than for TAV patients: BAV patients present with ascending aortic wall structural changes resulting in excessive stiffness and reduced compliance in comparison with patients with a normal TAV [71, 72]. In fact, a previous study reported a 109.8% increase in the aortic wall stiffness index for BAV patients in comparison with TAV ones [73]. However, these studies refer to the BAV population, not differentiating across phenotypes. Therefore, since the

available information on ascending aortic wall properties for BAV patients (and different phenotypes) is limited, the use of WSS to predict the possibility of damage to the aortic wall in specific categories, as well as regions of potential damage, can prove useful. This can be especially important for BAV type 2 patients, which have been computationally simulated here for the first time and have presented with presumably the most compromised mechanical and hemodynamic changes.

4.6 Limitations

Several limitations were present in this study. First, our aortic model presents with an in-plane curvature for the ascending portion, while a physiological aorta has typically an out-of-plane curvature. However, previous studies report that ascending aortic curvature can be seen as an independent risk factor for wall dissection or dilation onset [74], where a greater curvature is associated with worsened outcomes [75]. Since here we were focused on the comparison between BAV models, we chose an in-plane curvature aortic model.

Time-independency of the predictions was not assessed in this study; nonetheless, while parameters may reach convergence over a couple of cycles, any bias from such changes is expected to be consistent across the difference BAV phenotypes simulated. Further, we used direct validation against data available in literature to assess the accuracy of our models. Although only one systolic phase was modelled, consistent with a previous study [22], the same comparison was performed for all models, and so any trends are expected to be consistent across the simulations performed, not altering the ultimate conclusions from this proof-of-concept study.

In this study, blood flow was assumed to be laminar. In reality, the Reynolds number in the ascending aorta can reach values between 3000 and 3900 at peak systole, owing to the aortic valve opening and closure and the geometry of the aorta itself [76]. In BAV patients, the abnormal shape of the valve can lead to transitional blood flow, which might approach turbulent flow [77]. This is more likely the case for stenotic valves (such as the type 2 BAV). However, appropriate turbulence models for aortic flow have been identified as a current challenge [70, 77, 78], and may not be suitable for FSI problems [55, 79]. Critically, turbulence models may lead to very different predictions for WSS in healthy aortas which would likely not be appropriate for comparison to laminar flow models; for example, comparison of WSS and velocity for laminar and turbulence

models in an aortic aneurysm led to predictions which different by a factor of around $\times 2$ (data in supplementary material: [80]). In addition, a previous study employing laminar flow to study aortic valve calcification did not find a laminar flow model to limit the predicted results [26]. With such studies in mind, we do not view the use of a laminar model as leading to fewer limitations than the use of a turbulence model.

In this study, the aortic wall was assumed rigid. In reality, experimental data on the changes in ascending aortic wall material properties for BAV patients is currently limited. Incorporating a non-rigid wall would introduce a range of variables for which data is lacking; this would limit cross-BAV comparisons. In addition, previous studies have showed that the aortic wall in BAV patients presents with excessive stiffness and reduced compliance in comparison with patients with a TAV [71-73]. Hence, for these patients, it is preferable to assume the effect of wall motion in velocity and WSS fields as negligible [81]. Moreover, previous computational studies have noted that the essential characteristics of blood flow can be detected with the use of rigid wall models, for vessels such as the aorta [82]. Future studies assessing moving aortic walls would be beneficial, but characterisation of their mechanical properties needs to be evidence based and need to be specific to BAV phenotype.

Despite being anisotropic, valve tissue was assumed to follow linear, elastic and isotropic mechanical properties. Nonetheless, previous studies show that the physiological strain of aortic valve leaflets have a cyclical stretch of 10% [36-38]. In addition, the nonlinear stress-strain curve of the cardiac tissue can be approximated by two linear regions, where one occurs at low strain range (below 15%) and another happens at high strain rates [83]. At low strain rates, such linearity increases; therefore, given the reported range of cardiac tissue deformation in the aortic valve relevant to the simulations in our study, this assumption does not appear unjustifiable, and is consistent with previous studies [9, 15, 22, 39, 40]. Additionally, there is an inherent limitation in assigning anisotropic, and hyper-elastic material properties to cusps of BAVs in that characterisation of material properties of BAV cusps are not readily available in literature, and certainly not stratified according to phenotype.

The model used in this study employed an idealised pressure waveform (rather than patient specific [13, 84]) and no coupling with a lumped-parameter model for branching arteries was incorporated. However, there are challenges with tuning of the parameter values of a lumped parameter heart model [85]. Moreover, the aim of this proof-of-

concept study was the cross-comparison between TAV and BAV models which did not require a lumped-parameter model coupling. This aspect can be overcome in future studies; nonetheless, our model predictions are consistent with the clinical and experimental literature available. This is likely because primary flow through the ascending aorta is mostly undisturbed by excluding branching arteries.

6. Conclusion

BAV related haemodynamics and mechanics are altered in comparison with a TAV and different phenotypes yield different characteristics: type 0 BAV yields the least haemodynamic and mechanical impact, but its orifice orientation generates different magnitude and distribution of valve stress; type 1 BAVs present with similar quantitative haemodynamic and mechanical features across subtypes. Moreover, for the first time, a type 2 BAV was simulated computationally and our results suggest that this phenotype may be associated with greater valve and aortic damage in comparison with the other categories. These differences between and within categories of BAV may be central to subsequent pathology, including the location of such pathology. Our FSI model can therefore aid clinicians in patient risk stratification, estimating patients at a larger risk to develop complications derived from BAV abnormal haemodynamics and mechanics.

Conflicts of interest

The authors declare that they have no competing interests.

Funding details

No relevant funding.

Statement involving human and animal rights

No human or animal studies were carried out by the authors for this article.

References

1. Ward, C., *Clinical significance of the bicuspid aortic valve*. Heart, 2000. **83**(1): p. 81-5.
2. Robicsek, F., et al., *The congenitally bicuspid aortic valve: how does it function? Why does it fail?* Ann Thorac Surg, 2004. **77**(1): p. 177-85.
3. Sievers, H.H. and C. Schmidtke, *A classification system for the bicuspid aortic valve from 304 surgical specimens*. J Thorac Cardiovasc Surg, 2007. **133**(5): p. 1226-33.
4. Mahadevia, R., et al., *Bicuspid aortic cusp fusion morphology alters aortic three-dimensional outflow patterns, wall shear stress, and expression of aortopathy*. Circulation, 2014. **129**(6): p. 673-82.
5. Mirabella, L., et al., *MRI-based Protocol to Characterize the Relationship Between Bicuspid Aortic Valve Morphology and Hemodynamics*. Ann Biomed Eng, 2015. **43**(8): p. 1815-27.
6. Rodriguez-Palomares, J.F., et al., *Aortic flow patterns and wall shear stress maps by 4D-flow cardiovascular magnetic resonance in the assessment of aortic dilatation in bicuspid aortic valve disease*. J Cardiovasc Magn Reson, 2018. **20**(1): p. 28.
7. Sievers, H.H., et al., *Toward individualized management of the ascending aorta in bicuspid aortic valve surgery: the role of valve phenotype in 1362 patients*. J Thorac Cardiovasc Surg, 2014. **148**(5): p. 2072-80.
8. Markl, M., P.J. Kilner, and T. Ebbers, *Comprehensive 4D velocity mapping of the heart and great vessels by cardiovascular magnetic resonance*. J Cardiovasc Magn Reson, 2011. **13**: p. 7.
9. De Hart, J., et al., *A three-dimensional computational analysis of fluid-structure interaction in the aortic valve*. J Biomech, 2003. **36**(1): p. 103-12.
10. De Hart, J., et al., *A two-dimensional fluid-structure interaction model of the aortic valve [correction of value]*. J Biomech, 2000. **33**(9): p. 1079-88.
11. Spuhler, J.H., et al., *3D Fluid-Structure Interaction Simulation of Aortic Valves Using a Unified Continuum ALE FEM Model*. Front Physiol, 2018. **9**: p. 363.
12. Chen, Y. and H.X. Luo, *A computational study of the three-dimensional fluid-structure interaction of aortic valve*. Journal of Fluids and Structures, 2018. **80**: p. 332-349.
13. Bahraseman, H.G., et al., *Effect of exercise on blood flow through the aortic valve: a combined clinical and numerical study*. Computer Methods in Biomechanics and Biomedical Engineering, 2014. **17**(16): p. 1821-1834.
14. Bahraseman, H.G., et al., *Estimation of maximum intraventricular pressure: a three-dimensional fluid-structure interaction model*. Biomed Eng Online, 2013. **12**: p. 122.
15. Kuan, M.Y. and D.M. Espino, *Systolic fluid-structure interaction model of the congenitally bicuspid aortic valve: assessment of modelling requirements*. Comput Methods Biomech Biomed Engin, 2015. **18**(12): p. 1305-20.
16. Cao, K., et al., *Simulations of morphotype-dependent hemodynamics in non-dilated bicuspid aortic valve aortas*. J Biomech, 2017. **50**: p. 63-70.
17. Liu, J., J.A. Shar, and P. Sucosky, *Wall Shear Stress Directional Abnormalities in BAV Aortas: Toward a New Hemodynamic Predictor of Aortopathy?* Front Physiol, 2018. **9**: p. 993.

18. Kimura, N., et al., *Patient-specific assessment of hemodynamics by computational fluid dynamics in patients with bicuspid aortopathy*. J Thorac Cardiovasc Surg, 2017. **153**(4): p. S52-S62 e3.
19. Marom, G., et al., *Effect of asymmetry on hemodynamics in fluid-structure interaction model of congenital bicuspid aortic valves*. Conf Proc IEEE Eng Med Biol Soc, 2012. **2012**: p. 637-40.
20. Lavon, K., et al., *Fluid-Structure Interaction Models of Bicuspid Aortic Valves: The Effects of Nonfused Cusp Angles*. J Biomech Eng, 2018. **140**(3).
21. Hager, A., et al., *Diameters of the thoracic aorta throughout life as measured with helical computed tomography*. J Thorac Cardiovasc Surg, 2002. **123**(6): p. 1060-6.
22. Mohammadi, H., R. Cartier, and R. Mongrain, *The impact of the aortic valve impairment on the distant coronary arteries hemodynamics: a fluid-structure interaction study*. Med Biol Eng Comput, 2017. **55**(10): p. 1859-1872.
23. Mei, S., et al., *Hemodynamics through the congenitally bicuspid aortic valve: a computational fluid dynamics comparison of opening orifice area and leaflet orientation*. Perfusion, 2016.
24. Piatti, F., et al., *4D Flow Analysis of BAV-Related Fluid-Dynamic Alterations: Evidences of Wall Shear Stress Alterations in Absence of Clinically-Relevant Aortic Anatomical Remodeling*. Front Physiol, 2017. **8**: p. 441.
25. Oliveira, D., et al., *Bicuspid aortic valve aortopathies: An hemodynamics characterization in dilated aortas*. Comput Methods Biomech Biomed Engin, 2019. **22**(8): p. 815-826.
26. Halevi, R., et al., *Fluid-structure interaction modeling of calcific aortic valve disease using patient-specific three-dimensional calcification scans*. Med Biol Eng Comput, 2016. **54**(11): p. 1683-1694.
27. Bonow, R.O., et al., *ACC/AHA 2006 guidelines for the management of patients with valvular heart disease: a report of the American College of Cardiology/American Heart Association Task Force on Practice Guidelines*. J Am Coll Cardiol, 2006. **48**(3): p. e1-148.
28. Nishimura, R.A., et al., *2014 AHA/ACC guideline for the management of patients with valvular heart disease: a report of the American College of Cardiology/American Heart Association Task Force on Practice Guidelines*. J Am Coll Cardiol, 2014. **63**(22): p. e57-185.
29. van Loon, R., et al., *Comparison of various fluid-structure interaction methods for deformable bodies*. Computers & Structures, 2007. **85**(11-14): p. 833-843.
30. Shewchuk, J.R. *What is a Good Linear Element? Interpolation, Conditioning, and Quality Measures*. in *Eleventh International Meshing Roundtable*. 2002.
31. Belytschko, T., J.I. Lin, and C.S. Tsay, *Explicit Algorithms for the Nonlinear Dynamics of Shells*. Computer Methods in Applied Mechanics and Engineering, 1984. **42**(2): p. 225-251.
32. Hallquist, J., *LS-DYNA Keyword User's Manual*. 2006, Livermore Software Technology Corporation: LSTC, USA.
33. Carty, G., S. Chatpun, and D.M. Espino, *Modeling Blood Flow Through Intracranial Aneurysms: A Comparison of Newtonian and Non-Newtonian Viscosity*. Journal of Medical and Biological Engineering, 2016. **36**(3): p. 396-409.
34. Heuzé, O., *General form of the Mie-Grüneisen equation of state*. Comptes Rendus Mecanique, 2012. **340**: p. 679-687.

35. Wang, S.H., L.P. Lee, and J.S. Lee, *A linear relation between the compressibility and density of blood*. J Acoust Soc Am, 2001. **109**(1): p. 390-6.
36. El-Hamamsy, I., A.H. Chester, and M.H. Yacoub, *Cellular regulation of the structure and function of aortic valves*. J Adv Res, 2010. **1**: p. 5–12.
37. Ferdous, Z., H. Jo, and R.M. Nerem, *Strain magnitude-dependent calcific marker expression in valvular and vascular cells*. Cells Tissues Organs, 2013. **197**(5): p. 372-83.
38. Metzler, S.A., et al., *Cyclic strain regulates pro-inflammatory protein expression in porcine aortic valve endothelial cells*. J Heart Valve Dis, 2008. **17**(5): p. 571-7; discussion 578.
39. Luraghi, G., et al., *Does clinical data quality affect fluid-structure interaction simulations of patient-specific stenotic aortic valve models?* J Biomech, 2019. **94**: p. 202-210.
40. Wu, W., et al., *Fluid-Structure Interaction Model of a Percutaneous Aortic Valve: Comparison with an In Vitro Test and Feasibility Study in a Patient-Specific Case*. Ann Biomed Eng, 2016. **44**(2): p. 590-603.
41. Sturla, F., et al., *Impact of modeling fluid-structure interaction in the computational analysis of aortic root biomechanics*. Med Eng Phys, 2013. **35**(12): p. 1721-30.
42. Espino, D.M., D.E. Shepherd, and D.W. Hukins, *Evaluation of a transient, simultaneous, arbitrary Lagrange-Euler based multi-physics method for simulating the mitral heart valve*. Comput Methods Biomech Biomed Engin, 2014. **17**(4): p. 450-8.
43. Espino, D.M., D.E.T. Shepherd, and D.W.L. Hukins, *Transient large strain contact modelling: A comparison of contact techniques for simultaneous fluid-structure interaction*. European Journal of Mechanics B-Fluids, 2015. **51**: p. 54-60.
44. Barker, A.J., C. Lanning, and R. Shandas, *Quantification of hemodynamic wall shear stress in patients with bicuspid aortic valve using phase-contrast MRI*. Ann Biomed Eng, 2010. **38**(3): p. 788-800.
45. Barker, A.J., et al., *Bicuspid aortic valve is associated with altered wall shear stress in the ascending aorta*. Circ Cardiovasc Imaging, 2012. **5**(4): p. 457-66.
46. Bonomi, D., et al., *Influence of the aortic valve leaflets on the fluid-dynamics in aorta in presence of a normally functioning bicuspid valve*. Biomech Model Mechanobiol, 2015. **14**(6): p. 1349-61.
47. Dasi, L.P., et al., *Fluid mechanics of artificial heart valves*. Clin Exp Pharmacol Physiol, 2009. **36**(2): p. 225-37.
48. Bock, J., et al., *In vivo noninvasive 4D pressure difference mapping in the human aorta: phantom comparison and application in healthy volunteers and patients*. Magn Reson Med, 2011. **66**(4): p. 1079-88.
49. McNally, A., A. Madan, and P. Sucusky, *Morphotype-Dependent Flow Characteristics in Bicuspid Aortic Valve Ascending Aortas: A Benchtop Particle Image Velocimetry Study*. Front Physiol, 2017. **8**: p. 44.
50. Saikrishnan, N., et al., *In vitro characterization of bicuspid aortic valve hemodynamics using particle image velocimetry*. Ann Biomed Eng, 2012. **40**(8): p. 1760-75.
51. Becker, W., et al., *Bayesian sensitivity analysis of a model of the aortic valve*. J Biomech, 2011. **44**(8): p. 1499-506.

52. Lorenz, R., et al., *4D flow magnetic resonance imaging in bicuspid aortic valve disease demonstrates altered distribution of aortic blood flow helicity*. Magn Reson Med, 2014. **71**(4): p. 1542-53.
53. Burken, J., *Determining the effect of congenital bicuspid aortic valves on aortic dissection using computational fluid dynamics*, in *Biomedical Engineering*. 2012, The University of Iowa.
54. Chandra, S., N.M. Rajamannan, and P. Sucusky, *Computational assessment of bicuspid aortic valve wall-shear stress: implications for calcific aortic valve disease*. Biomech Model Mechanobiol, 2012. **11**(7): p. 1085-96.
55. Cao, K. and P. Sucusky, *Computational comparison of regional stress and deformation characteristics in tricuspid and bicuspid aortic valve leaflets*. Int J Numer Method Biomed Eng, 2017. **33**(3).
56. Gilmanov, A. and F. Sotiropoulos, *Comparative hemodynamics in an aorta with bicuspid and trileaflet valves*. Theoretical and Computational Fluid Dynamics, 2016. **30**(1-2): p. 67-85.
57. Kouhi, E. and Y.S. Morsi, *A parametric study on mathematical formulation and geometrical construction of a stentless aortic heart valve*. J Artif Organs, 2013. **16**(4): p. 425-42.
58. Richards, K.E., et al., *Influence of structural geometry on the severity of bicuspid aortic stenosis*. Am J Physiol Heart Circ Physiol, 2004. **287**(3): p. H1410-6.
59. Baumgartner, H., et al., *Echocardiographic assessment of valve stenosis: EAE/ASE recommendations for clinical practice*. Eur J Echocardiogr, 2009. **10**(1): p. 1-25.
60. Grimard, B.H. and J.M. Larson, *Aortic stenosis: diagnosis and treatment*. Am Fam Physician, 2008. **78**(6): p. 717-24.
61. Akins, C.W., B. Travis, and A.P. Yoganathan, *Energy loss for evaluating heart valve performance*. J Thorac Cardiovasc Surg, 2008. **136**(4): p. 820-33.
62. Manning, W.J., *Asymptomatic aortic stenosis in the elderly: a clinical review*. JAMA, 2013. **310**(14): p. 1490-7.
63. Butcher, J.T. and R.M. Nerem, *Valvular endothelial cells and the mechanoregulation of valvular pathology*. Philos Trans R Soc Lond B Biol Sci, 2007. **362**(1484): p. 1445-57.
64. Hamatani, Y., et al., *Pathological Investigation of Congenital Bicuspid Aortic Valve Stenosis, Compared with Atherosclerotic Tricuspid Aortic Valve Stenosis and Congenital Bicuspid Aortic Valve Regurgitation*. PLoS One, 2016. **11**(8): p. e0160208.
65. Conti, C.A., et al., *Biomechanical implications of the congenital bicuspid aortic valve: a finite element study of aortic root function from in vivo data*. J Thorac Cardiovasc Surg, 2010. **140**(4): p. 890-6, 896 e1-2.
66. Dolan, J.M., et al., *High fluid shear stress and spatial shear stress gradients affect endothelial proliferation, survival, and alignment*. Ann Biomed Eng, 2011. **39**(6): p. 1620-31.
67. Pasta, S., et al., *Difference in hemodynamic and wall stress of ascending thoracic aortic aneurysms with bicuspid and tricuspid aortic valve*. J Biomech, 2013. **46**(10): p. 1729-38.
68. Oliveira, D., et al., *Bicuspid aortic valve aortopathies: An hemodynamics characterization in dilated aortas*. Comput Methods Biomech Biomed Engin, 2019: p. 1-12.

69. Braunwald, E. and R.O. Bonow, *Braunwald's heart disease : a textbook of cardiovascular medicine*. 9th ed. 2012, Philadelphia: Saunders. xxiv, 1961 p.
70. Vergara, C., et al., *Influence of bicuspid valve geometry on ascending aortic fluid dynamics: a parametric study*. *Artif Organs*, 2012. **36**(4): p. 368-78.
71. Rooprai, J., et al., *Thoracic Aortic Aneurysm Growth in Bicuspid Aortic Valve Patients: Role of Aortic Stiffness and Pulsatile Hemodynamics*. *J Am Heart Assoc*, 2019. **8**(8): p. e010885.
72. Goudot, G., et al., *Aortic Wall Elastic Properties in Case of Bicuspid Aortic Valve*. *Front Physiol*, 2019. **10**: p. 299.
73. Nistri, S., et al., *Aortic elasticity and size in bicuspid aortic valve syndrome*. *Eur Heart J*, 2008. **29**(4): p. 472-9.
74. Poullis, M.P., et al., *Ascending aortic curvature as an independent risk factor for type A dissection, and ascending aortic aneurysm formation: a mathematical model*. *European Journal of Cardio-Thoracic Surgery*, 2008. **33**(6): p. 995–1001.
75. Gode, S., et al., *The role of the angle of the ascending aortic curvature on the development of type A aortic dissection: ascending aortic angulation and dissection*. *Interact Cardiovasc Thorac Surg*, 2019. **29**(4): p. 615-620.
76. Doorly, D. and S. Sherwin, *Geometry and flow*, in *Cardiovascular Mathematics: Modeling and simulation of the circulatory system*, L. Formaggia, A. Quarteroni, and A. Veneziani, Editors. 2009, Springer.
77. Faggiano, E., et al., *Helical flows and asymmetry of blood jet in dilated ascending aorta with normally functioning bicuspid valve*. *Biomech Model Mechanobiol*, 2013. **12**(4): p. 801-13.
78. Viscardi, F., et al., *Comparative finite element model analysis of ascending aortic flow in bicuspid and tricuspid aortic valve*. *Artif Organs*, 2010. **34**(12): p. 1114-20.
79. Cao, K. and P. Sucosky, *Effect of Bicuspid Aortic Valve Cusp Fusion on Aorta Wall Shear Stress: Preliminary Computational Assessment and Implication for Aortic Dilation*. *World J of Cardiovasc Dis*, 2015. **05**(06): p. 129-140.
80. Algabri, Y.A., et al., *Computational study on hemodynamic changes in patient-specific proximal neck angulation of abdominal aortic aneurysm with time-varying velocity*. *Australas Phys Eng Sci Med*, 2019. **42**(1): p. 181-190.
81. Simão, M., et al., *Aorta Ascending Aneurysm Analysis Using CFD Models towards Possible Anomalies*. *Fluids* 2017, 2(2), 31, 2017. **2**(31).
82. Formaggia, L., K. Perktold, and A. Quarteroni, *Basic mathematical models and motivations*, in *Cardiovascular Mathematics: Modeling and simulation of the circulatory system*, L. Formaggia, A. Quarteroni, and A. Veneziani, Editors. 2009, Springer.
83. Choudhury, N., et al., *Local mechanical and structural properties of healthy and diseased human ascending aorta tissue*. *Cardiovasc Pathol*, 2009. **18**(2): p. 83-91.
84. Bahraseman, H., et al., *Combining numerical and clinical methods to assess aortic valve hemodynamics during exercise*. *Perfusion*, 2014. **29**(4): p. 340-350.
85. Kim, H.J., et al., *On coupling a lumped parameter heart model and a three-dimensional finite element aorta model*. *Ann Biomed Eng*, 2009. **37**(11): p. 2153-69.
86. Alastruey, J., et al., *On the impact of modelling assumptions in multi-scale, subject-specific models of aortic haemodynamics*. *J R Soc Interface*, 2016. **13**(119).

87. Yap, C.H., N. Saikrishnan, and A.P. Yoganathan, *Experimental measurement of dynamic fluid shear stress on the ventricular surface of the aortic valve leaflet*. Biomech Model Mechanobiol, 2012. **11**(1-2): p. 231-44.
88. Chandran, K.B., S.E. Rittgers, and A.P. Yoganathan, *Biofluid mechanics : the human circulation*. 2007, Boca Raton: CRC/Taylor & Francis. 419 p.

Supplementary material

Fig. S1 Peak systolic velocity contours [m/s] at multiple horizontal section cuts (isometric view) for TAV, BAV type 0 anterior-posterior (AP), type 0 lateral, type 1 N-L, type 1 N-R, type 1 R-L, and type 2. Different velocity scales are used for the models, to better highlight secondary aortic flow patterns in each case.

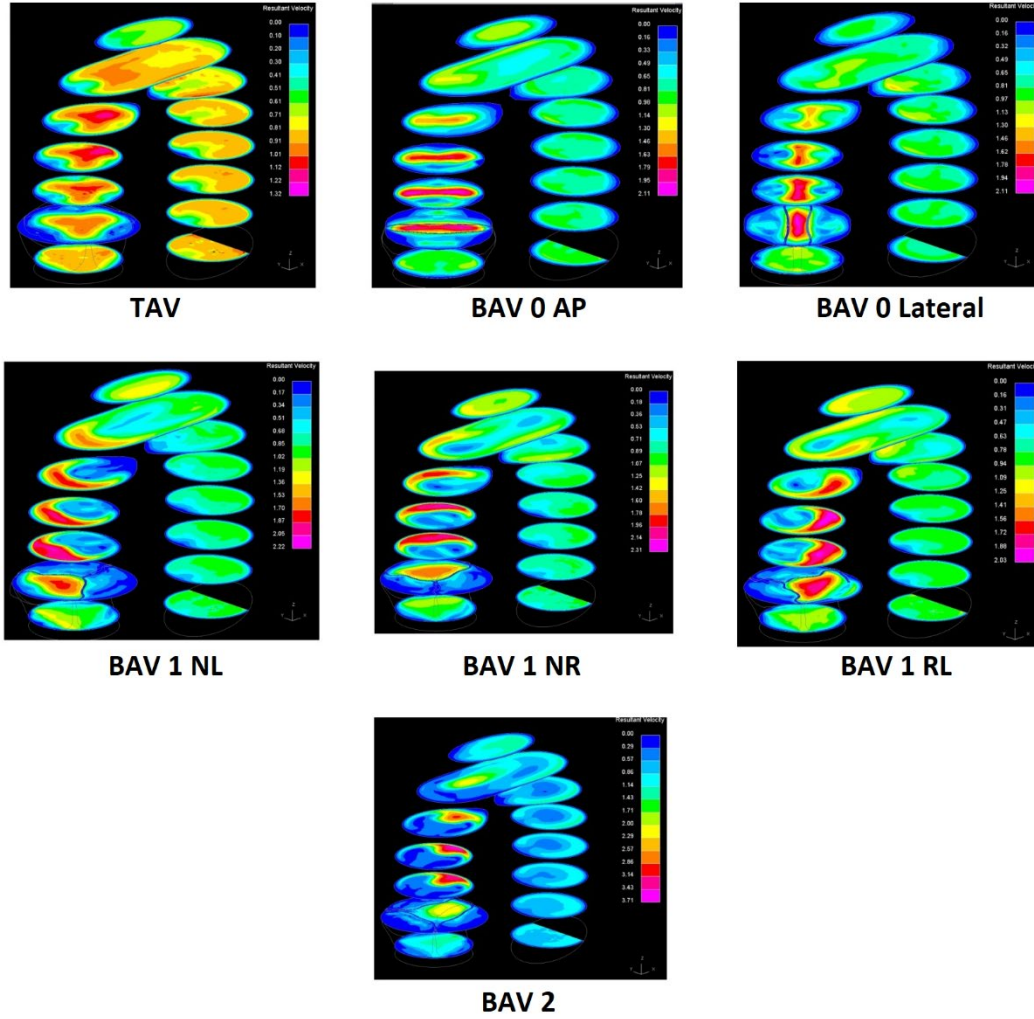


Fig. S2 Time-averaged WSS (TAWSS) at the B-B section for all models (full cardiac cycle).

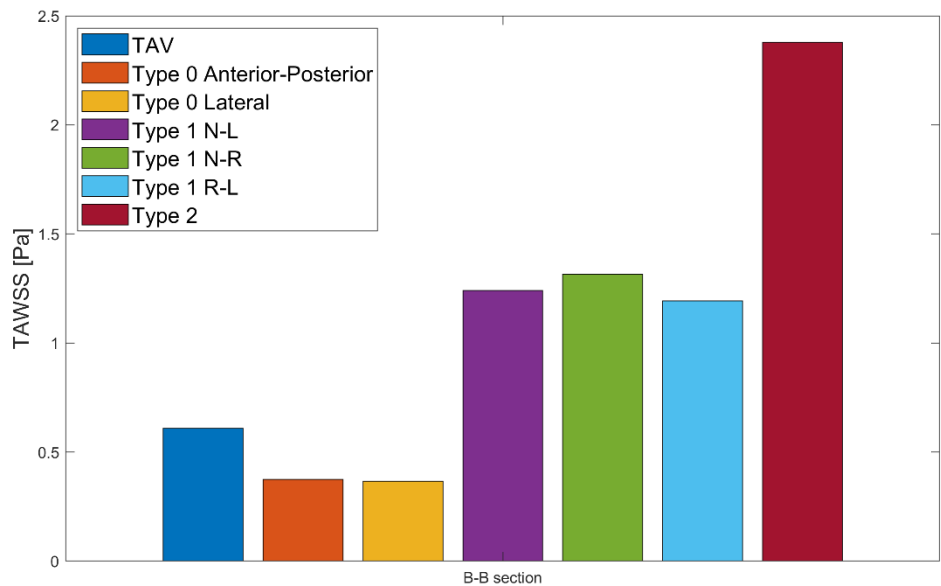
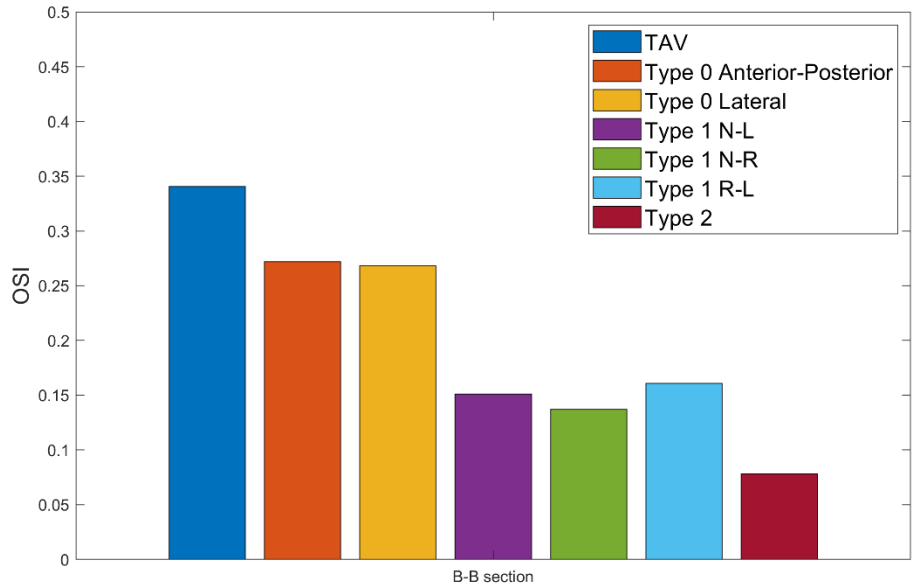


Fig. S3 Oscillatory shear index (OSI) at the B-B section for all models (full cardiac cycle).



Figures and tables for review (in order of citation on the text)

Table 1 Dimensions of BAV models (also see Fig. 2 and Fig. 3)

	TAV	BAV			
		Type 0 Anterior-Posterior	Type 0 Lateral	Type 1 N-L; N-R; R-L	Type 2
Sinus number	3	2	2	3	3
R_a (mm)	12.5	12.5	12.5	12.5	12.5
A_n (°)	118	180	180	138	138
A_l/A_r (°)	118	180	180	109	109
L_v (mm)	16.7	17.5	17.5	16.7	16.7
H_v (mm)	10.5	10.5	10.5	10.5	10.5
D_s (mm)	6	6	6	6	6
H_s (mm)	21	21	21	21	21

Notes: R_a , aortic radius; A_n , non-coronary cusp angle; A_l , left cusp angle; A_r , right cusp angle; L_v , non-coronary cusp arc length; H_v , cusp height; D_s , sinus depth; H_s , sinus height.

Fig. 1 BAV geometries. a) Type 0 anterior-posterior, b) type 0 lateral, c) type 1 N-L, d) type 1 N-R, e) type 1 R-L, f) type 2. Note: the raphe is highlighted with a black line

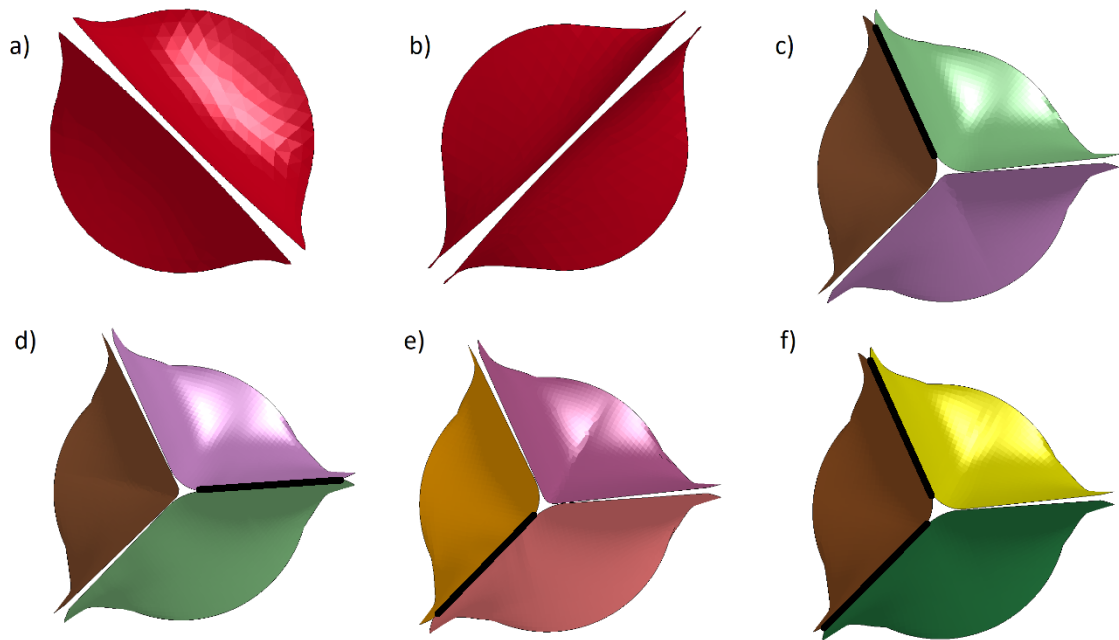


Fig. 2 Model dimensions, with a) view of the TAV leaflets and b) sagittal view of the model, including aortic root and ascending aorta. Notes: R_a , aortic radius; A_n , non-coronary cusp angle; A_l , left cusp angle; L_v , non-coronary cusp arc length; H_v , cusp height; D_s , sinus depth; H_s , sinus height

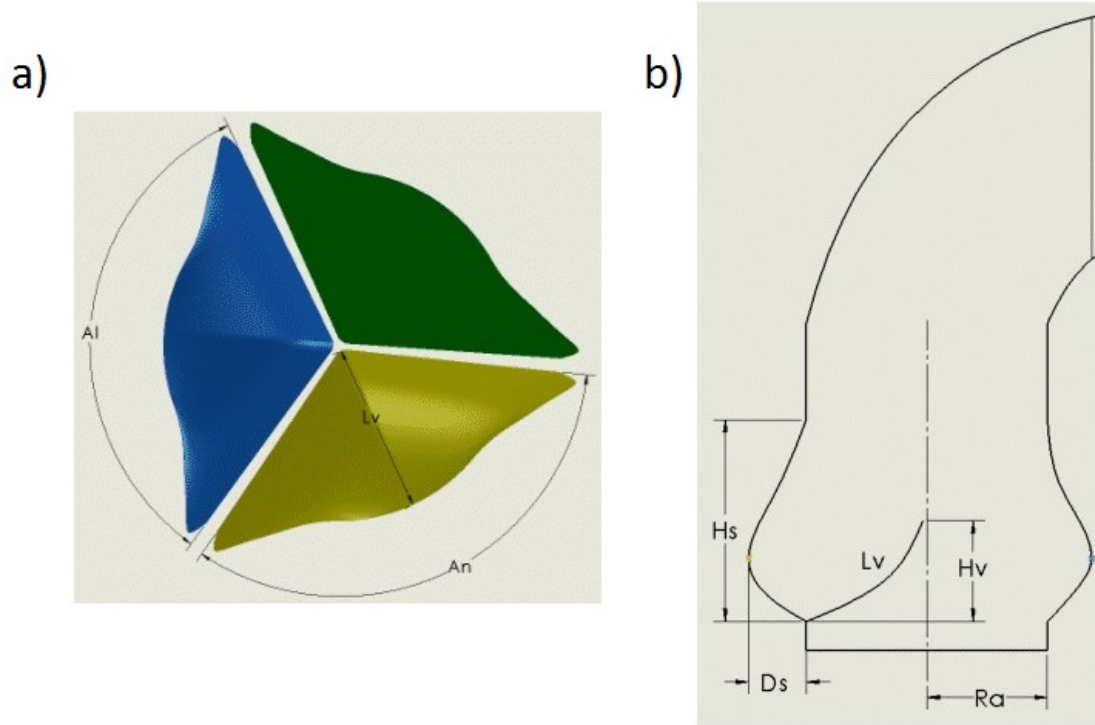


Fig. 3 Full aortic geometry, including a) mesh view of a complete aortic model with a TAV, b) coronal view with A-A cross-section, c) sagittal view, with B-B, C-C and D-D cross-sections. Note: Blue, green and yellow dots represent inlet, outlet and fixed constraint boundary conditions, respectively

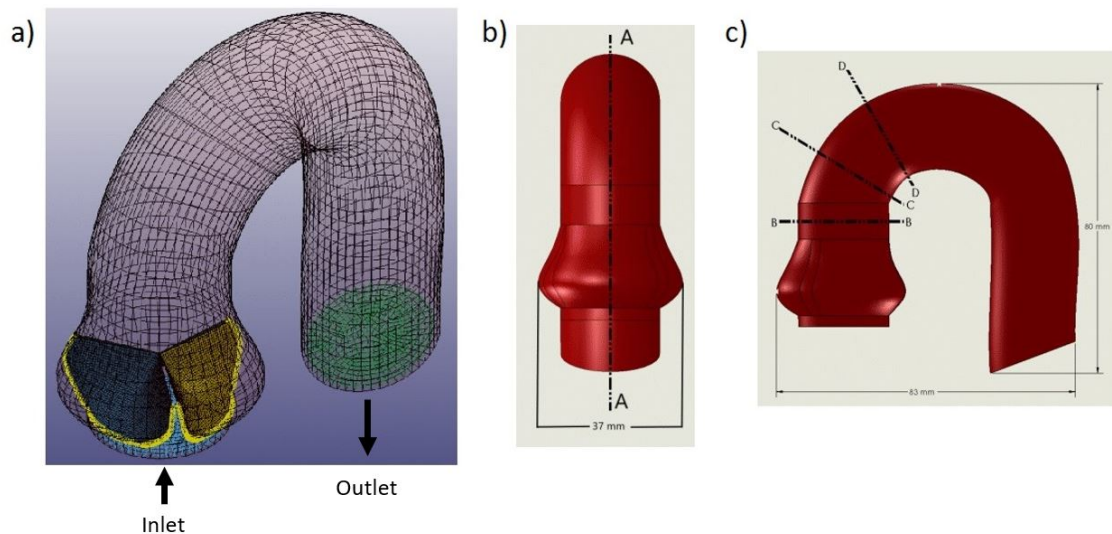


Fig. 4 Time-dependent boundary conditions imposed at the inlet (adapted from [78]) and outlet (adapted from [86]) boundaries

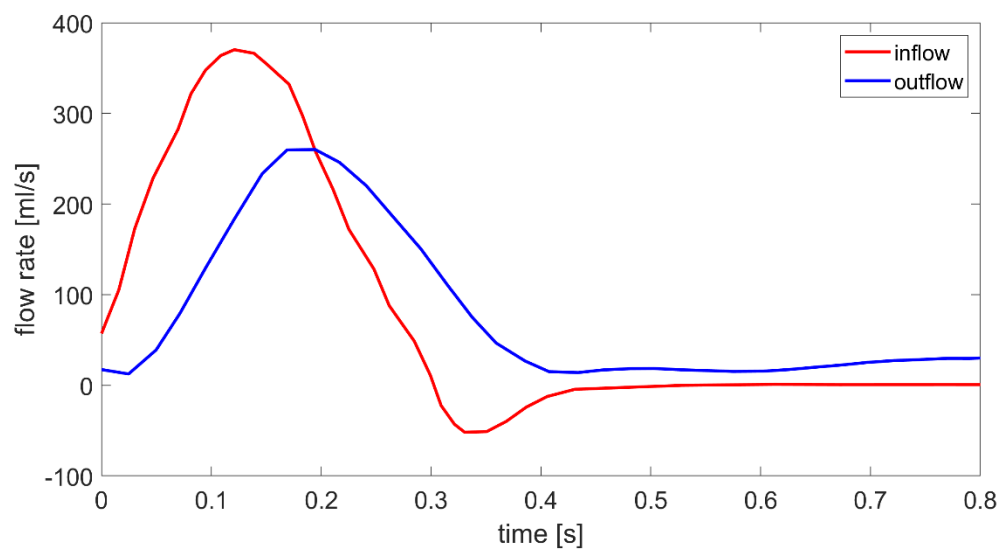


Fig. 5 Peak systolic velocity contours [m/s] at multiple horizontal section cuts (isometric view) for TAV, BAV type 0 anterior-posterior (AP), type 0 lateral, type 1 N-L, type 1 N-R, type 1 R-L, and type 2

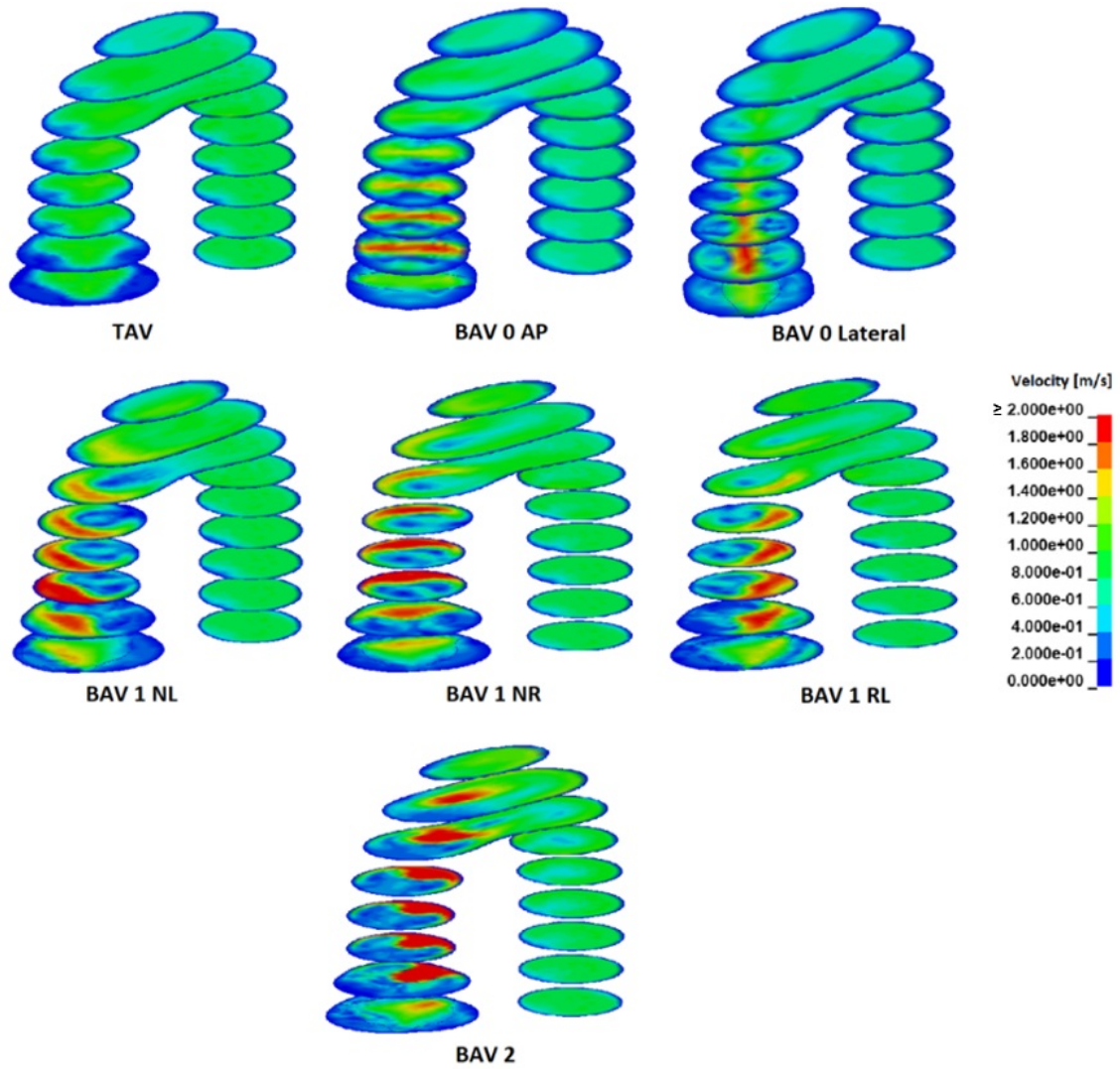


Table 2 Haemodynamic predictions from our computational model and literature results

	Prediction	TAV	BAV					
			Type 0 Anterior-Posterior	Type 0 Lateral	Type 1 N-L	Type 1 N-R	Type 1 R-L	Type 2
Peak velocity [m/s]	Our study	1.52	2.3	2.2	2.38	2.47	2.4	3.7
	<i>In vivo</i> [4-6]	0.9 – 1.8	-	-	-	-	2 – 3	-
	<i>In vitro</i> [49, 50, 87]	1.5 – 2.3	-	-	3.9	-	2.9 - 3.1	-
	<i>In silico</i> (CFD and FSI) [9, 15, 16, 23]	1.3 – 2.3	0.76 – 3.17	3.21	1.85	1.73	1.75	-
ΔP [mmHg]	Our study	4.5	15	15	13.1	14.3	15	37
	<i>In vivo</i> [48, 88]	< 10	-	-	-	-	-	-
	<i>In vitro</i> [50]	17.2	-	-	-	-	-	-
	<i>In silico</i> (CFD) [23]	5	22	22	-	-	-	-
FRR [%]	Our study	0	4.4	3.5	10.1	10.8	9.8	13.3
	<i>In vivo</i> [44]	0.3 – 0.9	-	-	-	-	-	-
	<i>In silico</i> (CFD) [46]	0	11.18	-	-	-	-	-
GOA [cm ²]	Our study	4.13	2	2.34	3.65	3.54	2.84	1.65
EOA [cm ²]	Our study	3.38	1.85	1.85	1.98	1.90	1.85	1.18
	Clinical guidelines [59-61]	Normal	Mild stenosis	Mild stenosis	Mild stenosis	Mild stenosis	Mild stenosis	Moderate stenosis

Fig. 6 Velocity vectors (m/s) at B-B section plane (top view) to show helix flow for TAV, BAV type 0 Anterior-Posterior, type 0 Lateral, type 1 N-L, type 1 N-R, type 1 R-L, and type 2. Note: BAV type 0 vectors are scaled in size, to be visible

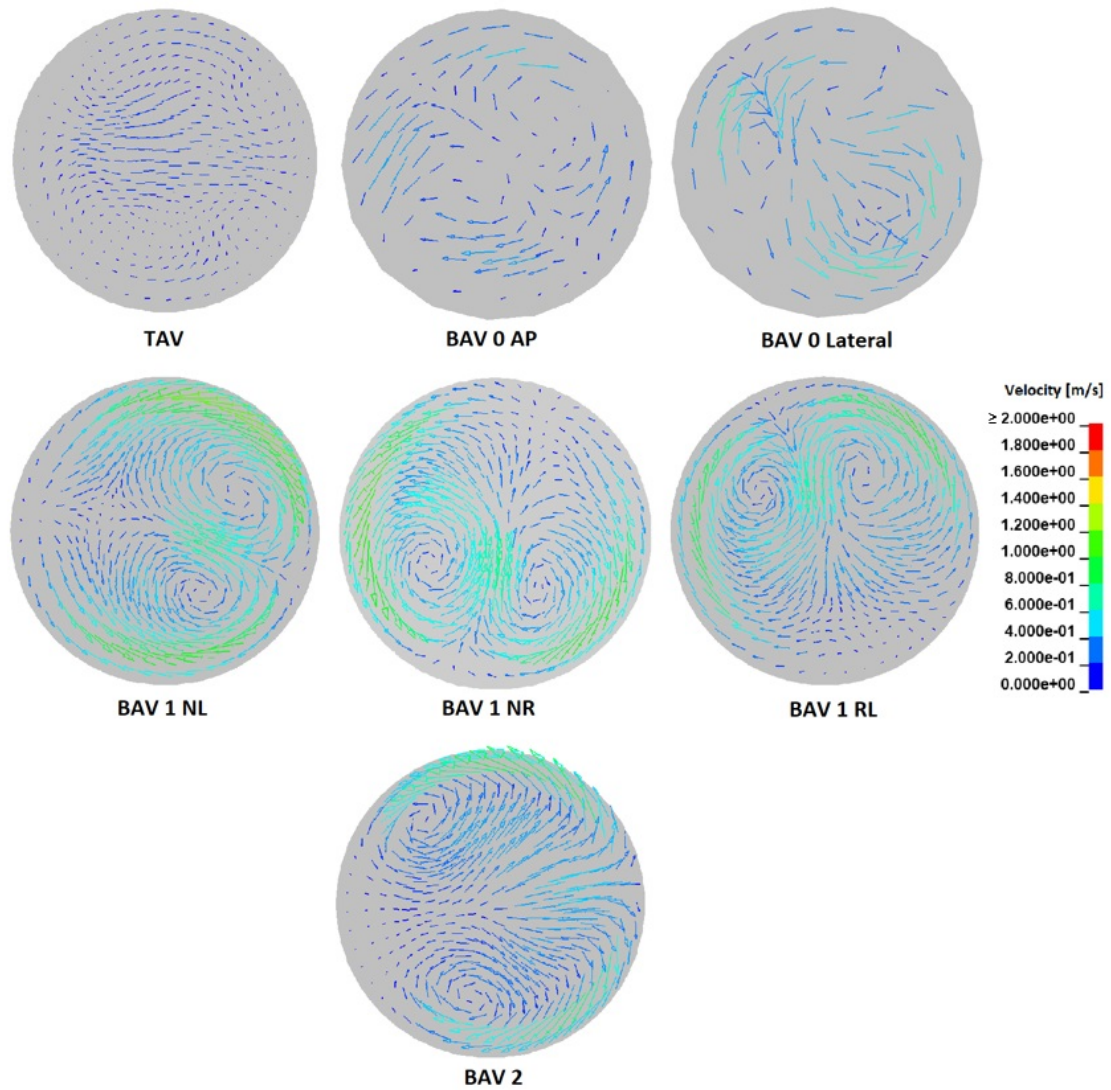


Table 3 Peak systolic stress predictions from our computational model and literature results

	Prediction	TAV	BAV					
			Type 0 Anterior- Posterior	Type 0 Lateral	Type 1 N-L	Type 1 N-R	Type 1 R-L	Type 2
WSS [Pa]	Our study	1.3	0.8	0.78	2.65	2.81	2.55	5.08
	<i>In vivo</i> [6, 45]	0.43 - 3	-	-	-	-	0.67 - 1	-
	<i>In silico</i> (CFD and FSI) [16, 17]	0.75 – 5			2.65	2.45	2.8	-
Von Mises stress [kPa]	Our study	300	270	600	590	630	610	1610
	<i>In silico</i> (CFD and FSI) [51, 57]	160 – 343	280		-	-	-	-

Fig. 7 Peak systolic WSS magnitude [Pa] at all cross-sections

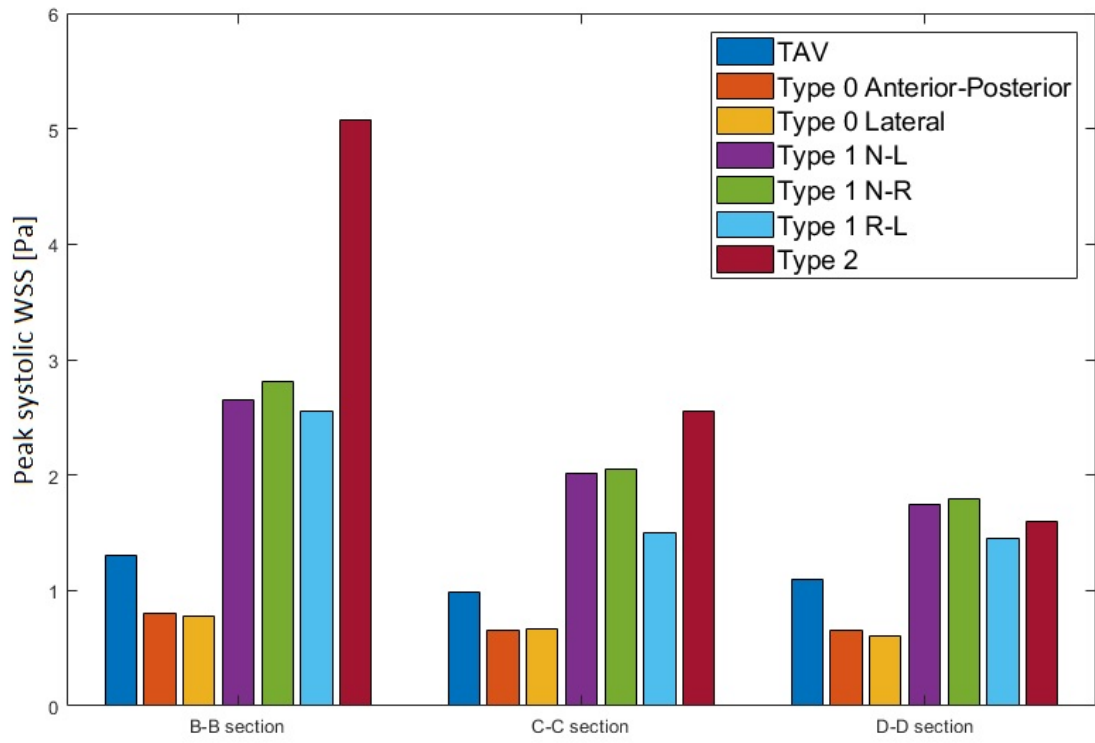


Fig. 8 Valve area-averaged Von Mises stress through the systolic phase

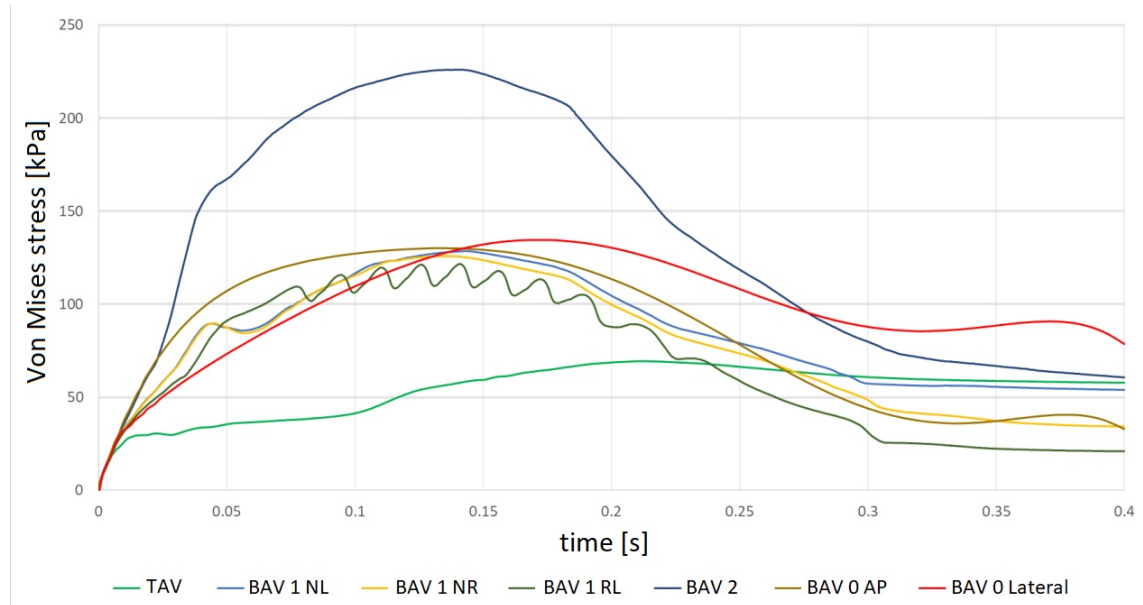


Fig. 9 Von Mises (Pa) stress contours at peak systole for TAV, BAV type 0 Anterior-Posterior, type 0 Lateral, type 1 N-L, type 1 N-R, type 1 R-L, and type 2

